POLITECNICO DI TORINO
Repository ISTITUZIONALE

A sensor for direct measurement of small convective heat fluxes: Validation and application to micro-structured surfaces

(Article begins on next page)

22 November 2024

A sensor for direct measurement of small convective heat fluxes: Validation and application to micro-structured surfaces

Eliodoro Chiavazzo[a], Luigi Ventola[a], Flaviana Calignano[b], Diego Manfredi[b], Pietro Asinari[a,*]

[a]*multi-Scale ModeLing Laboratory (SMaLL), Energy Department, Politecnico di Torino, Corso Duca degli Abruzzi 24, 10129 Torino, Italy*
[b]*Center for Space Human Robotics @Polito, Istituto Italiano di Tecnologia, Corso Trento 21, 10129 Torino, Italy*

Abstract

A sensor for measuring small convective heat flows ($<0.2\,\mathrm{W/cm^2}$) from micro-structured surfaces is designed and tested. This sensor exploits the notion of thermal guard and is purposely designed to deal with metal samples made by additive manufacturing, such as direct metal laser sintering (DMLS). For validation purposes, we utilize both experimental literature data and a computational fluid dynamic (CFD) model: Maximum and average deviations from CDF model in terms of the Nusselt number are on the order of $\pm 13.7\%$ and $\pm 6.3\%$, respectively while deviations from literature data are even smaller. Similar works in the literature often have the necessity of maintaining one-directional heat flows along the main dimension of a conducting bar using insulating materials. Such an approach can be critical for small fluxes due to the curse of heat conduction losses along secondary directions. As a result,

*corresponding author:
  Email address: pietro.asinari@polito.it (Pietro Asinari)
  URL: http://www.polito.it/small (Pietro Asinari)

it is necessary to estimate those secondary fluxes (e.g. by numerical models), thus making the measurement difficult and indirect. On the other hand, depending on the manufacturing accuracy, the present sensor enables to practically reduce at will those losses, with direct measurement of the heat flux. To our knowledge, the adoption of thermal guard is not a common practice in convective heat transfer, especially when local measurements are of interest. We hope that this study may (i) shed light on the usefulness of the approach in this field; and (ii) provide an effective tool for future investigation on electronic cooling and convective heat transfer enhancement by micro-/nano-structured surfaces. Owing to a number of features of the proposed device, we suggest that it can be prospectively utilized in the near future (i) for industrial applications (due to simplicity and robustness of the design); (ii) for high temperature measurements (unlike foil sensors, no delamination issues can be experienced); (iii) in the context of micro-electromechanical systems (MEMS) (easy to miniaturize).

Contents

List of symbols

A surface $[m^2]$

d cylinder diameter $[m]$

D hydraulic diameter $[m]$

h local convective heat transfer coefficient $[W/m^2/K]$

k sample-to-guard thermal transmittance $[W/K]$

l cylinder length $[m]$

L heating edge $[m]$

L_r reattachment length $[m]$

Nu   Nusselt number $[-]$

Pr   Prandtl number $[-]$

q generic independent quantity $[n.a.]$

q_{loss} conductive heat loss $[W]$

R electric resistance $[\Omega]$

Re   Reynolds number $[-]$

T temperature $[K]$

V potential difference $[V]$

v fluid velocity $[m/s]$

Q power generated by sample heater $[W]$

y^+ normalized dimensionless distance $[W]$

Δh centerline-to-average heat transfer coefficient correction term $[W/m^2/K]$

Greek symbols

ϵ emissivity $[-]$

λ thermal conductivity $[W/m/K]$

ν kinematic viscosity $[m^2/s]$

Σ standard uncertainties $[n.a.]$

$\Sigma_{h,B}$ type B standard uncertainties on h $[W/m^2/K]$

σ_B Stefan-Boltzmann constant $[W/m^2/K^4]$

$\sigma_{h,B}$ type B relative standard uncertainties on h $[\%]$

$\sigma_{h,A}$ type A relative standard uncertainties on h $[\%]$

σ_h overall relative standard uncertainties on h $[\%]$

Subscripts and superscripts

a	air
c	sample centerline
s	sample (sensor)
D	hydraulic diameter
f	G-10 fiberglass epoxy
$fluid$	FC-72 fluorocarbon liquid
g	guard (sensor)
$g1$	upstream guard (sensor)
$g2$	downstream guard (sensor)
h	heater
i	index of the i-th independent quantity
L	heating edge
q_i	i-th independent quantity
w	wall
ax	axial
av	average
m	adiabatic mixing
0	centerline-to-average correction term

1. Introduction

Measuring the convective heat transfer coefficient locally (i.e. on small ares on the order of 1 cm^2) usually presents difficulties, the reason being (among others) that such a quantity depends on both the flow regime and the fluid properties. Moreover, even though one assumes that the velocity bound-

ary layer is fully developed (which might not be the case for jets impinging on surfaces), still the local convective heat transfer coefficient strongly depends on the development of the thermal boundary layer. The latter remark is particularly relevant to electronics cooling. In fact, experiments on flush mounted heat sinks [1, 2, 3] clearly show that the local convection heat transfer coefficient is affected by the chip location on the electronic board. In particular, Authors in Ref. [1] found that the average convective heat transfer for the rows of heating arrays decreases approximately 25% from the first to the second row and by less than 5% from the third to the fourth row. Ref. [2] reports that, in steady state conditions, heat transfer coefficient is strongly affected by the number of chips and their locations in the streamwise flow direction. The latter results have been proved also in transient conditions [3]. The peak in the convective heat transfer coefficient at the edge of the heating surface is due to the small thickness of the thermal boundary layer in the early development region. Small thickness of the thermal boundary layer makes the developing region ideal to investigate the heat transfer enhancement due to micro- and nano-structures. For this reason, in the present paper, we will focus on a single flush-mounted heat source such as the one considered in [4].

Classical methods for measuring the local heat flow can be divided in three main categories: Methods based on thermography, on sensible capacitors and on diffusion meters [5]. During the past several years, infrared thermography has evolved into powerful tool to measure convective heat fluxes as well as to investigate the surface flow field over complicated bodies [6]. In spite of the advantages of the latter technique, e.g. the modest intrusiveness [7],

infrared thermography suffers from some drawbacks. First of all, the measurement accuracy depends on the knowledge of the emissivity coefficient of the surface exposed to the infrared camera [6]. This effect is more susceptible to highly polished surfaces: In fact, due to low emissivity coefficient and high reflectivity of the surface one has to cope with a low signal-to-noise ratio [6]. Moreover, surface structuring/patterning might create problems in estimating non-homogeneous emissivity. In case of electronic cooling with high packaging density, there might also be a problem in positioning the access window to the test surface for the infrared camera [6]. Finally, when measuring the local convective heat transfer coefficient over a fin, the temperature value identified at each image pixel by the infrared camera must be post-processed by a numerical model in order to estimate the desired quantity [8, 9]. Hence, it is an indirect measurement technique, which might be further affected by the uncertainties of the underlaying numerical model.

Measurements by sensible capacitors require that heat flow is used to transfer energy to a capacitor, where energy is stored in the form of sensible heat [5]. The heat flux is then measured by the time evolution of the temperature. Large thermal inertia is required, so that the time for thermal equilibrium is long and easily measurable. It is important that the temperature within the device is as uniform as possible and the volume/surface area ratio of the capacitor very small. Some disadvantages of sensible capacitors include inaccuracy in obtaining the time evolution of the temperature, the need to cool down the device to a temperature lower than the temperature where the heat flow is to be measured before measurements can be taken and the intrusiveness of the device [5].

On the other hand, diffusion meters are based on the Fourier's law of heat conduction at steady state [5]. Here, it is necessary that the heat flow within the device stays unidirectional. Consequently, some proper insulation must be ensured and the heat flux can be measured by a series of thermocouples installed along the main heat flow direction. Some disadvantages of diffusion meters include difficulties in maintaining the heat flow direction, the need for truly insulating layers around the measuring elements and the need for a steady-state measurement [5]. In addition, establishing an (easily) measurable temperature gradient in a highly conductive material requires large thermal fluxes. In case of forced air convection, thermal fluxes may be quite small (e.g. $< 0.2\ W/cm^2$) and this introduces significant difficulties in measuring a temperature gradient within a copper bar as in Ref. [4], where thermal fluxes larger than 5 W/cm^2 are indeed considered. Moreover, in case of small thermal fluxes, the relative magnitude of the conduction losses increases and it makes less accurate the measurement by a diffusive meter. We note that the conduction losses are, in general, non-linear. In fact, some thermal power is inevitably lost and reaches the air stream passing through the sensor holder. More dramatically, the amount of surface area which is crossed by conduction losses, is affected in turn by convection, thus making the thermal resistance due to conduction losses flow dependent. In our research activity, the latter issue was experienced during the development of a previous release of the presented sensor (not reported), and it was successfully solved by introducing the thermal guard. More details about the latter issue are provided below in Section 2.

Another type of sensor that has recently gained great popularity are flush

mounted sensors [10] [11], which are commonly used in heat transfer characterization of flat surfaces. However for micro-structured surfaces a reliable measure of the convective heat transfer coefficient is difficult to obtain with those sensors. In fact, if the latter sensors are mounted on micro-structured surfaces, then the fluid dynamics interactions between micro-structures and fluid flow are (at least locally) perturbed. This implies that heat transfer is altered by the presence of the sensor and hence the measurement is not reliable. On the other hand, positioning such sensors at the bottom of samples is not always an accurate solution, owing to an unavoidable change of the heat flux direction. Although one might think that the adoption of insulating materials (surrounding the sample facets that are not exposed to the fluid) represents an effective solution, in Section 2 we demonstrate that this may lead to non-negligible deviations in the heat flux estimates. In addition, the issue of undesired heat losses in such convective heat transfer measurements becomes even more serious when small fluxes are to be measured, thus making questionable the use of those sensors in the context of micro-electromechanical systems (MEMS), which is an active research area gaining and increasing popularity (see e.g. [11, 12]).

Motivated by all this, we have designed and validated (against both experimental data from literature and a computational fluid dynamic model) a sensor that is able to tackle the above drawbacks, by resorting to the notion of thermal guard. As a result, we summarize a few advantages of the proposed device which for our purposes (see samples in Section 6) could be hardly addressed by traditional approaches such as diffusion meters or flush mounted sensors:

1. The sensor does not perturb the fluid dynamic interactions between micro-structures and fluid flow.

2. The uncertainties due to (spreading) conduction losses can be effectively made negligible by adopting the thermal guard, which keeps the temperature within the device very uniform.

3. The experimental procedure is remarkably simple, because it only requires the measurement of an electrical power and three temperatures. No numerical model is required to post-process each time the measured quantities, leading to a direct measurement technique.

4. The sensor design can be miniaturized, making it an ideal candidate for studies with small heat fluxes (e.g. forced air convection and MEMS applications).

5. Unlike state-of-the-art flush mounted foil sensors, which are often limited in terms of the operating temperature due to delamination issues (i.e. 120-150 C°, see [13]), the present sensor can be easily designed to withstand high temperatures by a proper choice of materials.

The paper is organized as follow. The main traditional approaches for convective heat transfer measurements are reviewed in Section 1. In Section 2, the motivation of this study is presented by discussing the issue of spreading conduction losses when addressing the measurement of small heat fluxes by traditional devices. The key-idea behind the proposed sensor is presented in Section 3.1, whereas details about the sensor design are provided in Sections 3.2 and 3.3. In Section 4, the equipment and the procedure adopted in the validation process are discussed. In Section 5, the experimental results are presented and a comparison with both independent experimental data
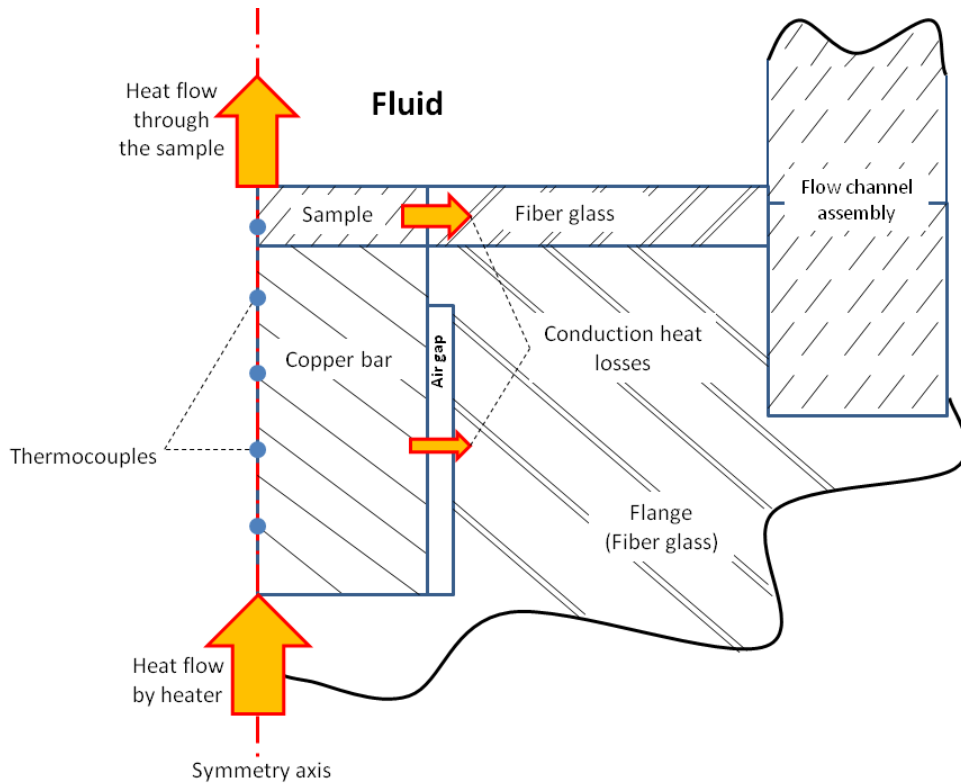
Figure 1: Example of a heat flow sensor as used in [4].

from literature and the results of a fluid dynamic model (whose details are discussed in the Appendix A) are reported. In Section 6, measurements of the heat transfer coefficient on prototypical micro-structured surfaces made by DLMS are shown. In Section 7, conclusions and perspectives are reported.

2. Motivation of the study

In the following, referring to the diffusion meter utilized in [4], we focus on possible issues arising when measuring small heat fluxes, as those experienced with low thermal conductive fluids (e.g. air) and/or small heat exchange

surface areas (e.g. small chips and/or MEMS devices). The device proposed in [4] is schematically reported in Fig. 1 and, similarly to our study below, utilizes a copper sample (with slightly different dimensions, namely $12.7 \times 12.7 \times 5.51 \ mm^3$) upon which the convective heat transfer coefficient is to be measured. The latter sample is flush mounted on one side of a flow channel, and surrounded by low thermal conductive G-10 fiberglass epoxy, for reducing conduction heat losses. Heat is generated by a cartridge heater positioned at the bottom of the bar and reaches the sample through a copper bar. The bar is embedded in a G-10 fiberglass flange. While an air gap is present along most of the bar length (roughly 30 mm), the remaining part of the bar (comparable to the sample thickness) is in direct thermal contact with the G-10 fiberglass epoxy. The temperature gradient (hence the heat flux) through the copper bar can be measured by means of four thermocouples located along the centerline of the copper bar. A linear trend of the temperature profile along the bar is demonstrated, hence the local heat flux at the copper bar axis can be accurately estimated by Fourier's law. Strictly speaking, owing to unavoidable conduction heat losses, the above heat flux is only accurate along the symmetry axis in Fig. 1. On the other hand, if the aim of the study is measuring the heat flow from the entire sample surface, the average heat flux is the quantity of interest. For instance, this is certainly true in electronics cooling, where the total dissipated heat from a chip surface is often the only concern. In those cases, the measurement accuracy of diffusion meters fully relies upon the possibility of neglecting the conduction heat losses (as compared to the heat flux exiting the sample surface exposed to the fluid flow) and on the assumption that the average

heat flux can be safely approximated by the value measured at the centerline. Whenever the above approximation does not hold, the use of correlations such as the one proposed in [4] (and derived from measurement along the copper bar centerline) clearly leads to overestimates of the average convective heat transfer. Towards an effort of quantifying the effect of the conduction heat losses in the experiments reported in [4], we invoke the following analytical formula expressing the conduction heat from a hot vertical cylinder (copper sample attached to the bar) embedded within a semi-infinite medium (air gap and G-10 fiberglass epoxy) (see Ref. [5] p. 224):

$$q_{loss} = \frac{2\pi l}{\ln(4l/d)}\lambda_f (T_s - T_a),$$
(1)

where l, d and λ_f denote the cylinder length, the cylinder diameter and the thermal conductivity of the fiberglass flange, respectively. The average convective heat transfer coefficient h over the sample surface can be cast into the form:

$$h = \frac{h_c L^2 (T_s - T_a) - q_{loss}}{L^2 (T_s - T_a)},$$
(2)

where h_c is the convective heat transfer coefficient at the centerline (consistently with the one measured in [4]). In the ideal case of $q_{loss} = 0$, it follows $h = h_c$. Owing to (1), the equation (2) reduces to the explicit expression:

$$h = h_c - \frac{2\pi l}{L^2 \ln(4l/d)}\lambda_f$$
(3)

By referring to Fig. 1, the cylinder presents a square cross-section and two different media are surrounding its mantel. To first approximation, even with a conservative assumption of neglecting the heat loss through the cylinder mantel facing the air gap, we have $l \approx l_f \approx 11\ mm$ with l_f being the cylinder

14

length in direct contact with the fiber glass. Finally, considering G-10 garolite [14] with $\lambda_f = 0.27 \; Wm^{-1}K^{-1}$ and an effective cylinder diameter $d = 14.3$ mm (chosen to preserve the heat transfer surface area by $L^2 = \pi d^2/4$), it yields the following estimate:

$$h \approx h_c - \Delta h, \tag{4}$$

with $\Delta h = 103 \; Wm^{-2}K^{-1}$. In [4] an empirical correlation is provided for samples with a smooth surface:

$$Nu_L^c = 0.237 Re^{0.608} Pr^{1/3}, \tag{5}$$

where the superscript in the Nusselt number Nu_L^c is used to stress that this quantity is based on measurements of h_c: $Nu_L^c = h^c L / \lambda_{fluid}$. In particular, because an inert flourocarbon liquid (FC-72) is used in the work of Maddox & Mudawar, the correction term Δh in equation (4) can be translated in terms of a corresponding Nusselt number as follows:

$$Nu_L^0 = \frac{\Delta h L}{\lambda_{fluid}} \approx \frac{103[Wm^{-2}K^{-1}] \, 0.0127[m]}{0.057[Wm^{-1}K^{-1}]} = 22.9, \tag{6}$$

and consequently the following dimensionless group:

$$\frac{Nu_L^0}{Pr^{1/3}} = \frac{40.1}{12.3^{1/3}} = 9.9, \tag{7}$$

where the Prandtl number is assumed to be $Pr = 12.3$ (see also Fig. 6 in Ref. [4]). As a result, if the average heat transfer coefficient h is of interest (instead of h_c), the correlation (5) should be expressed as follows:

$$\frac{Nu_L + Nu_L^0}{Pr^{1/3}} = 0.237 Re^{0.608}, \tag{8}$$

15

where $Nu_L = hL/\lambda_{fluid}$ and $Nu_L^c = Nu_L + Nu_L^0$. It is worth stressing that the above analysis aims at providing only an estimate of the conduction heat losses for the set-up in Fig. 1. Hence, for the sake of simplicity, the contact thermal resistance between the cylinder and the surrounding medium has been neglected to first approximation. As a consequence, (7) is expected to slightly overestimate the group $Nu_L^0/Pr^{1/3}$. However, judging from (7), in the low Reynolds numbers regime (e.g. $Re \approx 3000$) and for the analyzed configuration, the influence of the correction term Nu_L^0 can be on the order of $0.35\ Nu_L^c$. Hence, as long as the average convective heat transfer coefficient is of interest, there are certainly conditions where conduction losses cannot be neglected and should be properly taken into account during the measurement process. The above argument also shows that, due to difficulties in evaluating the correction term (7) with a desired accuracy (e.g. owing to possible unpredictable thermal contact resistances), the use of diffusion meters (or other sensors suffering from conduction heat losses) in such a context may become quite problematic.

For the sake of completeness, we also constructed a computational fluid dynamic (CFD) model to compute the average convective heat transfer coefficient through a square shaped sample (consistently with the set-up of interest for our study). Details of the model are reported in the Appendix A. Most importantly, we note that the latter numerical model is found to be in good accordance with the empirical correlation proposed by [4], and here re-formulated in terms of the Nusselt number based on the average convective heat transfer coefficient following Eq.(8). The comparison in reported in Fig. 2, where the adoption of a linear vertical scale (instead of the usual

logarithmic one) makes the matching even more appreciable. Hence, as long as smooth samples are concerned, we have both an experimental correlation (8) and numerical results from CFD for validating the proposed sensor.

We also stress that, although the above discussion focused on conduction heat losses in a diffusion meter, a similar analysis also applies to devices where a flush mounted foil sensor is adopted for instance between the bar and the sample. In fact, reducing at will the heat losses through the finite thickness of the sample (e.g. by means of insulating materials) is not a trivial task, especially when the fluid thermal conductivity is comparable to (or even smaller than) the adopted insulating material.

On the other hand, in our applications (discussed in Section 6) involving samples similar to the ones shown in Figs 7, different types of traditional sensors present other drawbacks (see for instance the discussion in Section 1).

As a result, in this work, we were encouraged to design a new sensor for the direct and accurate measurement of the average convective heat transfer coefficient over small surfaces. In the presented implementation, the sensor is conceived for dealing with forced air cooling a sample surface (roughly 1 cm^2), and details are reported in the sections below.

In principle, there are no limitations to a further miniaturization of the sensor. As mentioned in Ref. [11], such a feature is highly desirable and still represents a challenge for state-of-the-art flush mounted foil sensors.

3. Design of a new sensor

3.1. The key idea

The key-idea is to exploit the notion of thermal guard for local convective heat transfer measurements. Guarded hot plate method has been extensively used in measuring thermal conductivity. When attaching two thermostats at different temperatures to the opposite faces of the sample, heat flows from the hot to cold side typically following three-dimensional paths. However, a one-dimensional flow can be established within a sample by surrounding it with temperature-controlled "guards" designed to prevent the heat flow in all directions other than the desired one [15].

The ability of the guard to prevent undesired heat flows can be conveniently used for measuring convective heat transfer coefficients as well. Sensors based on this concept may be so accurate that can be used even for calibration purposes. For instance, the US National Institute of Standards and Technology (NIST) has developed a convective heat flux facility to allow calibration of heat flux sensors based on a guarded calibration plate ($30\,cm \times 10\,cm \times 3\,cm$) [16]. Another example of thermal guard based heat transfer coefficient sensors can also be found in [17].

Our main goal is to follow a similar idea at a smaller scale, and use it beyond calibration purposes for developing a simple though accurate sensor. An isometric view of the proposed sensor is reported in Fig. 3. The proposed sensor is made of three essential parts: (i) sample, (ii) insulation shield and (iii) guard. A heater is placed at the bottom of the sample and the latter is made of highly conductive material, because it has to efficiently transfer heat towards the flushing flow. The sensor presents an onion-like structure:

18

Insulation shield wraps the sample, while a highly conductive guard wraps the assembly consisting of both the sample and the insulation shield. The insulation shield and the guard are shaped such that the guard sharply joins the sample, and the sensor surface exposed to the air flow appears as a unique element. As a result, we obtain two independent thermal circuits, where the sample heater generates the thermal power to be removed by the tested surface, while an auxiliary heater supplies thermal energy to the guard until isothermal condition is reached (i.e. negligible heat transfer between the guard and the sample).

3.2. Mechanical design

Fig. 3 shows the sample (in our realization, a box of $11.1\,mm \times 11.1\,mm \times 5\,mm$), which is heated at the bottom and cooled from above by air flushing in a wind tunnel. The top surface of the sample can be possibly patterned in order to investigate different techniques for heat transfer enhancement. The sensor sample is heated by an electrical heater (a $12.7\,mm \times 12.7\,mm$ Minco heater with a nominal resistance of $26.5\ \Omega$). Thermal grease, with conductivity $2.9\,W/m/K$, was used for reducing thermal resistances at all contact surfaces of the device, when appropriate. The sample is surrounded by an insulation shield made of Teflon. This element consists of a $16\,mm \times 16\,mm \times 3\,mm$ plate at the bottom and a $2.4\,mm$-thick square-shaped tapered ring with negligible thickness at the test surface. Finally, the sample and shield assembly is embedded within the thermal guard which comprises a square-shaped complement of the insulation shield on top of a flat plate. The latter two elements are made of copper and their mechanical and thermal contact is ensured by two watch screws (M1.6). The upper part of the guard is built by

19

electro-erosion in order to have sharp edges leading to minimal sample/guard contact (important for having two independent thermal circuits). The guard heater (same electrical resistance by Minco is used) is positioned upstream for (partially) compensating the higher convective heat transfer coefficient due to the development of the thermal boundary layer (induced by the guard). The sensor assembly is held by an insulator holder made of nylon, which is fixed to the wind tunnel (discussed below).

Three temperatures are measured by means of Chromel-Alumel (type K) thermocouples with probe sheath diameter of 0.5 mm. A first thermocouple crosses all layers and reaches the center of the sensor sample. The remaining two thermocouples are inserted in the upstream and downstream wall, respectively. Although the development of the thermal boundary layer might lead to small temperature differences streamwise, we found that having three thermocouples in a row aligned along the fluid flow is twofold advantageous. First, this enables to check that only a minimal temperature differences is established between two sufficiently far locations of the guard (in our setup, on the order of 0.2 K). Second, imposing that the sample temperature T_s is the arithmetic mean of the two temperature values in the guard, namely $T_s = (T_{g1} + T_{g2})/2$, enables to minimize the net heat exchange between sample and guard due to possible balance mismatches.

3.3. Computational support to design

The design process has been assisted by numerical computations. In particular, a three-dimensional numerical model has been developed and solved by Fluent™. A simplified non-coupled model solves the stationary energy balance equation within the sensor assembly, assuming a fixed convective heat

20

transfer coefficient.

Let us suppose to use copper (thermal conductivity 388 $W/m/K$) for both the sample and the guard, Teflon™ (0.25 $W/m/K$) for the insulation shield and nylon (0.25 $W/m/K$) for the external sensor holder. This model includes the convective heat transfer as a boundary condition on the surface in contact with the flushing flow. A fixed convective heat transfer coefficient is assumed for both the sample and the guard, namely 70 $W/m^2/K$. The back side of the sensor is subject to a different boundary condition due to natural convection with a coefficient of 10 $W/m^2/K$.

In the model, the thermal power of the sample heater and the one of the guard heater can be independently controlled. Let us suppose to provide 0.05 W to the sample heater. The balance condition will be defined by matching the sample temperature T_s, measured at the sample center, and the guard temperature T_g, measured in the guard lateral wall, up to a certain precision. Let us suppose that $T_s - T_g = 0.2\,K$ and consequently that part of the power provided by the sample heater flows towards the guard. The numerical model can be used to evaluate the power lost towards the guard. In our set-up, it was found to be 0.002 W), corresponding to 4 % of the sample heater power. Hence, by linear extrapolation, the conduction losses towards the guard can be expressed as $k\,(T_s - T_g)$ where $k = 0.01\,W/K$.

It is worth stressing that the transmittance k depends on the sensor geometry, hence it is only required to be computed once for ever (for a given sensor design).

4. Use of the sensor in a wind channel

4.1. Experimental equipment

The flow loop of the experimental system is schematically shown in Fig. 4. The developed sensor is installed at the center of the vertical wall of a horizontal rectangular flow channel, which resembles a small open-loop wind tunnel. The channel has a smooth inner surface, a cross section of $228\,mm \times 158\,mm$ (hydraulic diameter $187\,mm$) and an entrance length of $5\,m$ (corresponding roughly to 26 hydraulic diameters). The air is blown by a Savio s.r.l. centrifugal fan type SFL 25-A (maximum flow rate $70\,m^3/min$ at $420\,Pa$, maximum pressure difference $1900\,Pa$ at $18\,m^3/min$), with a throttling valve for regulating the mass flow rate. At the end of the channel, downstream from the test section, a vane anemometer Testo 450 by Testo AG (sensitivity $\pm 0.1\,m/s$) was used for measuring the axial velocity. The air temperature is measured at the same location where the anemometer is installed (not affected by the power released by the convective sensor). The thermocouple probe sheath is embedded in a block of polystyrene foam, covered by an aluminum foil, ensuring stable measurements and negligible effects due to radiation. Similarly, the channel wall temperature is measured by a thermocouple installed on the inner surface of the channel, covered by a block of polystyrene foam with an external aluminum foil. Also in this case, Chromel-Alumel (type K) thermocouples were used. Two HQ PS3003 variable power suppliers (voltage range $0-30\,V$ and $0-3\,A$) are used to feed both the sample and the guard heater. Finally, a six-digits, electronic multimeter (Agilent 34401A) is used to measure the voltage to the sample heater circuit, made of the heater itself and the wires to connect the heater

22

to the power supplier.

4.2. Experimental procedure

The axial velocity v_{ax}, measured by the vane anemometer, is used to compute the Reynolds number $\mathrm{Re}_D^x = v_{ax} D/\nu$ where D is the hydraulic diameter of the channel. We note however that, the experimental data are usually reported in terms of a differently defined Reynolds number $\mathrm{Re}_D = v_{av} D/\nu$, which depends on the average velocity v_{av} instead. These two velocities have been correlated by a purposely-developed fluid dynamic numerical model, which was solved by Fluent™and described in the Appendix A. The previous numerical model was used to construct the following relation, $\mathrm{Re}_D = 0.694 \, (\mathrm{Re}_D^x)^{1.0162}$, which correlates the average velocity to the axial velocity (measured by the vane anemometer) through the corresponding Reynolds numbers.

For computing the average convective heat transfer coefficient at the sample surface, the following relation is used

$$h = \frac{V_h^2/R_h - \sigma_B \epsilon A(T_s^4 - T_w^4) - k[T_s - (T_{g1} + T_{g2})/2]}{A(T_s - T_a)}, \qquad (9)$$

where V_h is the potential difference across the sample resistance, R_h is the sample resistance, $\sigma_B = 5.67 \times 10^{-8} \ W/m^2/K^4$ is the Stefan-Boltzmann constant, ϵ is the emissivity of the sample surface, T_s is the sample temperature measured by the thermocouple inserted in the center of the sample, T_w is the temperature of the channel wall, $k = 0.01 \ W/K$ is the sample-to-guard coupling transmittance (see Section 3.3), T_{g1} and T_{g2} are the temperatures measured by the (upstream and downstream) thermocouples installed into the thermal guard, $A = 1.23 \ cm^2$ is the flat sample surface (even in case of

23

micro-structures) and, finally, T_a is the air temperature. V_h is calculated by the following equation:

$$V_h = V \frac{R_h}{R_h + R_{wire}},$$

(10)

where V is the voltage applied to the sample heater circuit, measured by the multimeter for each test, while R_{wire} is the resistance of heater wires, which measures 0.015 Ω. Before proceeding with the experimental results, a discussion about the estimate of uncertainties and their propagation by the proposed measurement chain is required. Eqs. (9) and (10) allow to compute h as a function of other measurements $(V, T_s, T_{g1}, T_{g2}, T_a, T_w)$ and parameters $(R_h, R_{wire}, \epsilon)$, namely $h = h(V, T_s, T_{g1}, T_{g2}, T_a, T_w; R_h, R_{wire}, \epsilon)$. These independent quantities can be organized in a vector, namely

$$\boldsymbol{q} := \{V, T_s, T_{g1}, T_{g2}, T_a, T_w; R_h, R_{wire}, \epsilon\},$$

where $q_i \in \boldsymbol{q}$ denotes the generic i-th quantity. The type B standard uncertainty (coverage factor: 2) of the quantity h, namely $\Sigma_{h,B}$, can be computed by the following uncertainty estimation method [19]:

$$\Sigma_{h,B} = \frac{1}{h} \sqrt{\sum_{i=1}^{9} \left(\Sigma_{q_i} \frac{\partial h}{\partial q_i} \right)^2},$$

(11)

where Σ_{q_i} is the standard uncertainty for the quantity q_i. Instead of assuming the nominal value of R_h (namely 26.5 Ω), the value of the sample resistance has been measured as function of the sample temperature (thermal drift), in order to obtain the functional dependence $R_h = f(T_s)$. Hence Eqs. (9) and (10) are based on the measured potential difference only. The standard uncertainty of the voltage measured by the multimeter can be assumed

24

Σ_V=0.0016 V. The temperatures T_s, T_{g1} and T_{g2} are critical and, therefore, thermocouples calibrated by thermostatic bath were used. The corresponding uncertainties can be assumed $\Sigma_{T_s} = \Sigma_{T_{g1}} = \Sigma_{T_{g2}} = 0.05$ K. On the other hand, other thermocouples might be characterized by $\Sigma_{T_a} = \Sigma_{T_w} = 0.4$ K, because of the intrinsic uncertainties of the installation setup. We have chosen $\Sigma_{R_h} = \Sigma_{R_{wire}} = 0.014\Omega$. Anemometer calibration has been performed and corresponding uncertainty has been calculated. The latter depends on measured velocity according to a polynomial function. Minimum and maximum calculated values of uncertainty $\Sigma_{v_{ax}}$ are 0.1 m/s and 0.38 m/s respectively.

The estimate of the sample surface emissivity ϵ requires more care, and the following procedure is adopted. The sample temperature was measured first by the calibrated thermocouple. Next, the surface emissivity was tuned by a thermal camera (NEC TH9100 Series Infrared Thermal Imaging Camera), in order to match the latter (independently) measured temperature. This procedure provided $\epsilon = 0.23$ and 0.1 for copper and aluminum alloy AlSi10Mg, respectively (below the reason for characterizing also AlSi10Mg is clarified). We decided to assume a quite large value of uncertainty, i.e. $\Sigma_\epsilon = 0.1$, owing to the poor quality of the infrared image. In table 1, uncertainties of measured quantities and sensitivities of measurement devices used in this work are reported.

Using the above values of standard uncertainties Σ_{q_i}, type B uncertainty $\Sigma_{h,B}$ has been calculated through Eq. (11); Consequently, the type B relative standard uncertainty $\sigma_{h,B}$ has been calculated by $\sigma_{h,B} = \Sigma_{h,B}/h_F$, where h_F is a power-law least squares fitting of the experimental data for each sample.

Table 1: measured quantities uncertainties and measurement devices sensitivities

Measured quantity	Σ_{qi}	Device	Sensitivity
V	0.0016 V	Multimeter (voltage measurement)	0.00001 V
T_s	0.05 K	Thermocouple	0.041 mV/K
T_{g1}	0.05 K	Thermocouple	0.041 mV/K
T_{g2}	0.05 K	Thermocouple	0.041 mV/K
T_a	0.4 K	Thermocouple	0.041 mV/K
T_w	0.4 K	Thermocouple	0.041 mV/K
R_h	0.014 Ω	Multimeter (resistance measurement)	0.0001 Ω
R_{wire}	0.014 Ω	Multimeter (resistance measurement)	0.0001 Ω
ϵ	0.1	Thermal camera	0.08 K
v_{ax}	0.1−0.38 m/s	Vane anemometer	0.1 m/s

In particular, $h_F = h_F(v_{av}) = d_1 v_{av}{}^{d_2}$, where d_1 and d_2 are proper fitting parameters.

On the other hand, a novel method has been proposed in this work for calculating type A uncertainties. This method aims to take advantage of measurements performed at different velocities to properly calculate tolerance intervals [18, 20]. Given a set of n measurements of convective heat transfer coefficients h_i, performed at different velocities v_i, the latter have been normalized with regards to the corresponding power-law fitting, namely $h'_i = h_i/h_F(v_i)$. Consequently, a new set composed by n elements h'_i has been obtained and we found that they are distributed according a Gaussian function. Hence, the mean value μ' and the standard deviation σ' of the latter set can be computed. Finally, the population mean μ and the maximum population standard deviation σ of the set can be calculated by the Student's t-distribution and the Chi-squared distribution, respectively. In particular, $\mu = \mu' \pm \sigma_\mu$, where $\sigma_\mu = t_{1-\alpha/2,\,n-1}\,\sigma'/\sqrt{n}$ and $\sigma = \sigma'/\chi_{\alpha/2}\sqrt{n-1}$ [19]. Combining the previous standard deviations, namely $\sigma_{h,A} = \sqrt{\sigma_\mu^2 + \sigma^2}$, we obtain

$$\sigma_{h,A} = \sigma' \sqrt{\frac{t_{1-\alpha/2,\,n-1}^2}{n} + \frac{n-1}{\chi_{\alpha/2}^2}}. \tag{12}$$

Finally, the overall relative standard uncertainty can be obtained as

$$\sigma_h = \sqrt{\sigma_{h,A}^2 + \sigma_{h,B}^2}. \tag{13}$$

It is worth to highlight that the previous procedure allows one to compute tolerance intervals, which are wider than confidence intervals and more robust estimates of the experimental uncertainty. Anticipating the experimental results described in Section 5, the maximum and mean relative uncertainty

27

for the convective heat transfer coefficient is $\pm9.9\%$ and $\pm6.7\%$, respectively. Moreover, in our experiments, A-type uncertainty is wider than B-type uncertainty (the latter being $\pm2\%$), proving that the overall accuracy of the measurement procedure is satisfactory.

Values of type A uncertainties depend on the number of experimental tests n (See Eq. 12). In particular, they are supposed to decrease as n increases (See Ref. [18]). Finally, a comprehensive statistical analysis of experimental data must include a procedure able to detect outliers in the data sets. In this study Grubb's test has been used to identify outliers among extreme data. For our particular data sets no outliers have been found, hence no data have been canceled out. The latter result proves good repeatability of the proposed sensor.

5. Sensor validation

In this section, experimental results are reported in order to validate the proposed sensor. In particular, 15 and 13 experimental points were investigated for aluminum alloy AlSi10Mg and copper samples smooth surfaces respectively, by varying the axial velocity in the range $3.1-15.5\ m/s$. We chose to test a sample made of AlSi10Mg in order to make sure that the proposed sensor can properly function with samples made of a different material compared to the guard. In particular, AlSi10Mg has a thermal conductivity of $150\ W/m/K$, which is roughly one-third compared to copper, and is often used in DLMS application [18]. Experimental points are reported in Tables 2 and 3. The sample heater thermal power in the proposed experiments is roughly $0.126\ W$ (corresponding to power densities of $0.102\ W/cm^2$). The

Table 2: Experimental data about convective heat transfer for AlSi10Mg sample.

v	Re_L	T_s	T_a	$\frac{V_h^2}{R_h}$	h	$\frac{Nu_L}{Pr^{1/3}}$	σ_h
$[\frac{m}{s}]$	$[-]$	[℃]	[℃]	$[W]$	$[\frac{W}{m^2K}]$	$[-]$	$[\%]$
3.3	3493	61.9	29.2	0.1271	30.80	26.47	6.55
4.2	4528	57.9	29.1	0.1271	35.10	30.17	5.97
5.2	5585	54.0	29.0	0.1270	40.58	34.88	5.48
6.2	6659	51.1	29.3	0.1270	46.75	40.17	5.14
7.2	7747	48.0	28.7	0.1270	52.67	45.27	4.88
8.2	8843	46.7	28.2	0.1270	54.95	47.23	4.79
9.2	9944	45.0	27.5	0.1269	58.08	49.91	4.69
9.2	9944	44.0	27.3	0.1275	60.96	52.39	4.65
10.3	11159	43.2	27.3	0.1274	64.24	55.21	4.59
10.3	11159	43.4	27.7	0.1273	65.00	55.86	4.58
11.3	12263	42.2	27.3	0.1274	68.85	59.17	4.52
12.2	13256	41.1	27.3	0.1273	74.19	63.76	4.46
13.2	14357	40.1	27.2	0.1273	79.07	67.96	4.42
14.2	15454	39.4	27.3	0.1273	84.75	72.83	4.38
15.1	16549	38.9	27.3	0.1274	88.97	76.47	4.36

Table 3: Experimental data about convective heat transfer for copper sample.

v	Re_L	T_s	T_a	$\frac{V_h^2}{R_h}$	h	$\frac{Nu_L}{Pr^{1/3}}$	σ_h
$[\frac{m}{s}]$	$[-]$	[°C]	[°C]	$[W]$	$[\frac{W}{m^2K}]$	$[-]$	$[\%]$
3.1	3289	62.0	29.2	0.1248	28.74	24.70	8.42
3.3	3493	62.7	29.1	0.1259	28.23	24.26	8.50
3.8	4111	58.0	29.3	0.1241	33.63	28.90	8.32
4.8	5160	52.0	27.4	0.1253	38.94	33.47	8.63
6.3	6768	48.5	27.9	0.1254	47.48	40.80	9.33
8.8	9503	42.5	27.2	0.1261	64.70	55.61	8.55
8.8	9503	44.5	28.6	0.1253	62.16	53.42	8.79
10.1	10938	42.6	27.5	0.1244	64.93	55.81	9.77
12.2	13256	40.2	26.9	0.1254	74.70	64.20	8.54
13.0	14137	39.6	27.1	0.1255	79.84	68.62	8.58
14.1	15345	39.1	27.1	0.1257	83.01	71.34	9.85
14.9	16330	39.3	28.4	0.1251	91.99	79.06	8.52
15.1	16549	37.3	26.3	0.1264	91.68	78.79	8.30

power densities are quite small (due to air), which make accurate measurement pretty challenging. For each test, the thermal power supplied to the guard is adjusted in order to satisfy the following condition at steady state: $T_s = (T_{g1} + T_{g2})/2$. During our tests, the thermal balance was found to be well satisfied: For the upstream part of the guard, the average temperature difference $T_{g1} - T_s$ is $0.19\ K$ (maximum $0.40\ K$) while, for the downstream part, the average temperature difference $T_s - T_{g2}$ is $0.23\ K$ (maximum $0.40\ K$).

Experimental data are reported in Fig. 5, where they are compared to both an experimental correlation from literature [4] (with conduction losses properly taken into account by Eq. (8)) and numerical results from CFD model (see the Appendix A for details). As visible in Fig. 5, the accordance of our experimental results with the two chosen benchmarks is good. Maximum and average deviations from CFD model are 13.7% and 6.3%, respectively, whereas the same devations with respect to literature [4] are 10.7% and 3.4%, respectively. The results of copper and aluminum alloy are consistent, showing that the proposed sensor can operate with samples made of different materials (as long as the thermal conductivity is high enough to ensure a uniform temperature field).

In Fig. 6, we report the result of additional experimental tests where the power supplied to the sample is the varying parameter, in order to understand the optimal heat flux for the measurement. In this case, we fixed the flow velocity, which is equal to 3.4 m/s at the channel axis. Standard theoretical arguments require that a variation of the supplied power should not affect the value of the convection heat transfer coefficient, meaning that the supplied

power is expected to show a linear behavior with respect to temperature difference.

This is confirmed in Fig. 6, where a linear best fit reveals a positive supplied power for a null temperature rise, defined as the difference between the temperature of the sample and that of air: $T_s - T_a$. However, we would expect that such a linear correlation passes through the origin of axes (i.e. no temperature difference is observed when the power supplier is off). This evidence can be explained as follows. All the measurements are based on the air temperature at the channel axis, see Eq. (9). However, in the present case, there is a small temperature difference between the air flowing inside the wind tunnel and the environment, because of the irreversibilities caused by the blower. The blower increases air temperature of roughly $2\,K$, and this generates a temperature difference between air and the channel walls. While air flows through the channel, the portion of air flushing close to the walls is cooled down by the walls. On the contrary, the air flowing at the channel axis experiences a weaker cooling. At the test section, the air thermal profile is slightly non-uniform: namely, air temperature at channel axis is slightly higher than the temperature of air flushing on the sample. When the latter is at the same temperature of the air flowing at the channel axis (the difference $T_s - T_a = 0\,K$), the sample is warmer than air passing in its close proximity and a small thermal power removal is observed (See Fig. 6).

Now we examine the experimental data shown in Table 2 and 3 in order to estimate how much this phenomenon affects the measurements reliability. At the test section, the temperature difference between air and walls is highly variable, with a maximum recorded value of $1.78\,K$ and a minimum one of

0.16 K. This means that slightly different thermal boundary layers showed up at the test section during the experimental campaign. This fact may have an effect on the measurement of the average convective heat transfer, as it is directly influencing the considered T_a at the denominator of Eq. (9). Instead of using the air temperature at the channel axis, i.e. T_a, one could use a proper corrected value, namely the adiabatic mixing temperature T_m, in Eq. (9), taking into account the actual temperature profile. For each experimental data shown in Table 2 and 3, one could estimate two values of h by setting $T_m = T_a$ (thus obtaining the value of h shown in Fig. 5) or $T_m = T_w$. Calculating the relative errors, defined as the differences between the h values calculated using $T_m = T_a$ and the h values calculated using $T_m = T_w$, we found a maximum and an average relative error equal to $\pm 2.6\%$ and $\pm 1.5\%$, respectively. The latter values are much smaller than the estimated overall measurement uncertainties, namely $\pm 9.9\%$ and $\pm 6.7\%$. Hence it is possible to assume that the above phenomenon has a negligible effect for value of the heat flux equals or higher than those used in our experiments (i.e. $Q \geq 0.126\,W$), corresponding to a power density of ≥ 0.102 W/cm^2. The present release of the sensor works in range of $0.102 - 3.100$ W/cm^2, where the maximum power density depends on the adopted heater. Maximum working temperatures are also estimated to be equal to $50 - 100$ Celsius for previous power densities. It is worth to point out that the above maximum working temperature and power density are mainly limited by the chosen heater, as well as by the present selection of materials. These thresholds can be easily overcome by proper design choices, without changing the main idea of the proposed sensor.

6. Measuring local convective heat transfer of micro-structured surfaces

6.1. Examples of micro-structured surfaces

The sensor described in this work has been designed to measure the convective heat transfer coefficient of small micro-structured surfaces (on the order of 1 cm^2). In Fig. 7 a few examples of such surfaces are shown. Those are made by direct metal laser sintering (DMLS), trade name for EOS GmbH process, which can build full dense parts with mechanical properties equivalent or even superior to those of parts produced by conventional manufacturing [21, 22]. Moreover, the surface morphology of these parts can also be tuned (to some extent), in order to produce artificial roughness with desired thermal features. More details about the potential impact of DMLS on convective heat transfer enhancement and manufacturing parameters have been reported elsewhere [18].

In particular, the sample shown in Fig. 7(a) is a surface with cubic pin fins with 2 mm edges, which represents a classical macroscopic solution. The one shown in Fig. 7(b) is a modified version of the previous one. Inside each pin fin, a Venturi-like nozzle has been fabricated, aiming at generating a velocity component orthogonal to the main flow direction (see also the cross-section reported in Fig. 8 as an example). The expected working principle is shown in Fig. 9: The fluid, after passing through the Venturi nozzle, experiences wall flow separation. The flow is expected to reattach to the wall after a certain length (known as reattachment length L_r). Until the reattachment length is not reached, flow near the walls typically presents rotating eddies. Hence, a velocity component orthogonal to the main flow

direction is obtained. Because of its geometrical features, obtained exploiting the capability of DMLS technique, we call this example micro-structured surface. The sample shown in Fig. 7(c) is a flat rough surface, where the surface morphology has been induced by modifying the standard DMLS parameters [18]. Finally, Fig. 7(d) shows a sample made of a macroscopic fin (height equal to 10 mm), but with quite rough surfaces. The latter can be considered a simple example of a hierarchical geometry, where micro-structures (i.e. artificial roughness) are planned in top of a macroscopic fin [18]. As mentioned above, a reliable measure of the convective heat transfer coefficient of these kind of surfaces is difficult to obtain with flush mounted sensor [10] [11]: Hence they are representative test cases, where the proposed sensor can be beneficial.

6.2. Measurement of micro-structured surface local convective heat transfer

The convective heat transfer of classical pin fins and Venturi-like pin fins are measured by the proposed sensor and reported in Figs. 7(a) and (b). Four samples have been tested, namely two classical solutions made of eight and thirteen pin fins, and their corresponding Venturi-like versions, namely with a nozzle embedded in each fin. Each Venturi-like sample has been tested in both convergent and divergent configuration by inverting the flow direction: more precisely, by referring to Fig. 9, in the convergent configuration air flows from right to left, while in the divergent configuration, air flows in the opposite direction. Venturi-like pin fins were expected to have a higher convective heat transfer coefficient than classical pin fins. This expectation was based on the idea that air flowing in a convergent nozzle should accelerate thus producing a velocity component orthogonal to the main flow direction,

35

Table 4: Heat transfer surface areas of considered samples and their normalizations by $A = 1.123 \times 10^{-4}\ m^2$.

Number of pins	A	classical		Venturi-like	
$[-]$	$[m^2]$	$[m^2]$	w.r.t. A	$[m^2]$	w.r.t. A
8	1.23×10^{-4}	2.51×10^{-4}	2.04	3.23×10^{-4}	2.62
13	1.23×10^{-4}	3.31×10^{-4}	2.69	4.48×10^{-4}	3.64

because of the downward eddies (see Fig. 9). Moreover, a further increase would be expected by the increase in the total heat transfer surface area, as shown in Table 4.

Result of the tests are shown in Fig. 10. The reference area used for the calculation of h by Eq. (9) is the flat sample area which is the same for all, i.e. $A = 1.123 \times 10^{-4}\ m^2$. In both convergent and divergent configuration, Venturi-like pin fins have roughly the same heat transfer performance compared to the corresponding sample with classical fins. This result may be explained by assuming that a negligible amount of air flows through the nozzles. Consequently additional area due to their internal surfaces do not significantly contribute to convective heat transfer, and hence there is no effective velocity component orthogonal to the main flow. On the other hand, the convective heat transfer scales by the the number of pin fins, as expected.

Even though the Venturi-like pin fins do not show heat transfer enhancement, the key point of this section is to provide a practical example about how the proposed sensor can be used to asses the thermal performance of small micro-structured surfaces. Different successful solutions based on

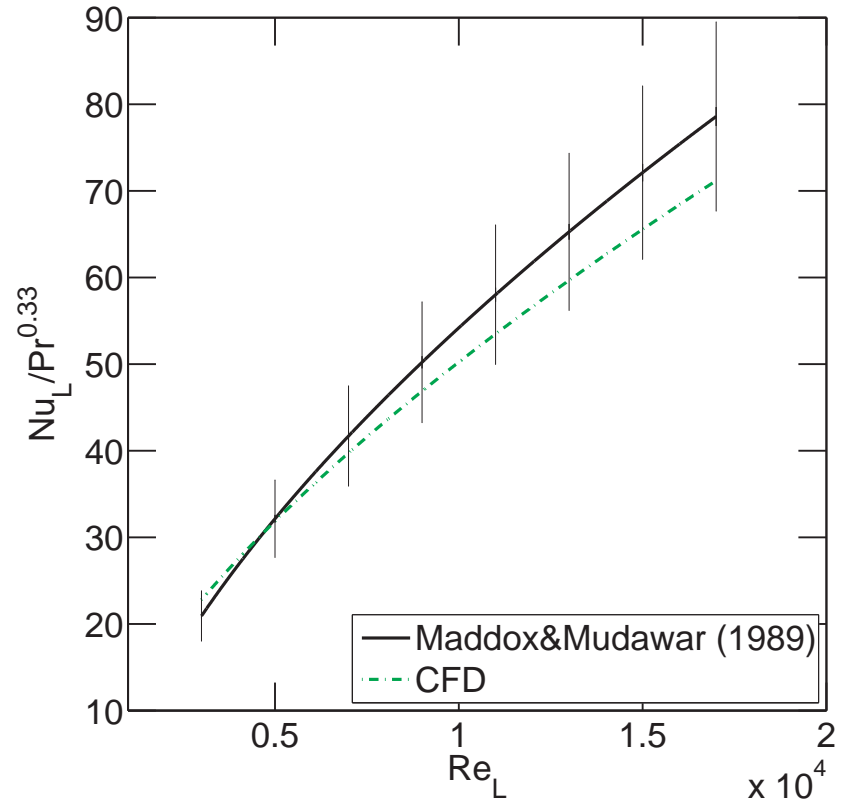micro-structures surfaces can be found in Ref. [18].

Figure 2: Maddox&Mudawar experimental correlation [4] re-formulated in terms of Nusselt number based on the average convective heat transfer coefficient according to the Eq. (8) (solid line) vs the CFD results (dot-dashed). Error bars with amplitude $\pm$ 13.9 % are shown as vertical bars for the Maddox&Mudawar experimental correlation.
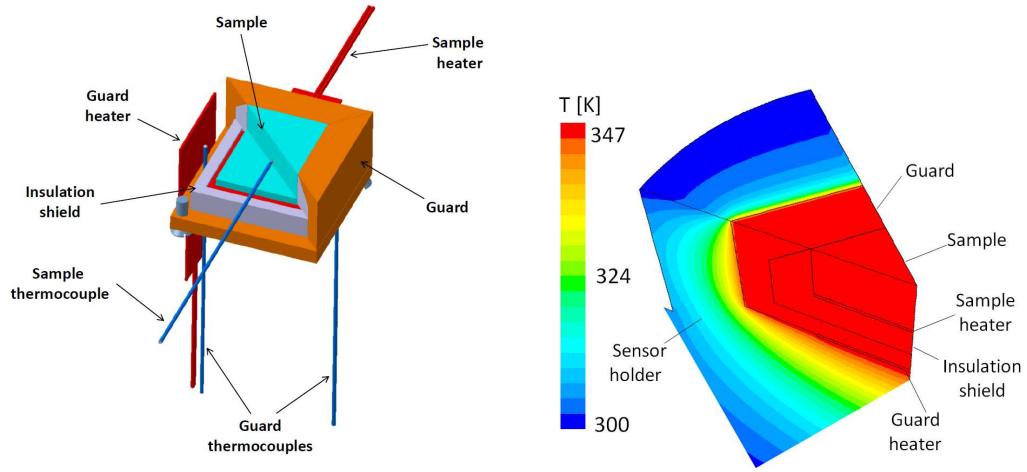
Figure 3: (Color on-line). Left-hand side: Isometric view of the proposed sensor. Right-hand side: The design process has been assisted by a three-dimensional numerical model solving the energy balance equation. This model is particularly useful to compute the sample-to-guard coupling transmittance k. To this purpose, the guard heater location does not play a crucial role (k mainly depends on the sensor geometry), and particularly in the model the heater is placed at the bottom of the guard, while in the isometric view it is displayed laterally.
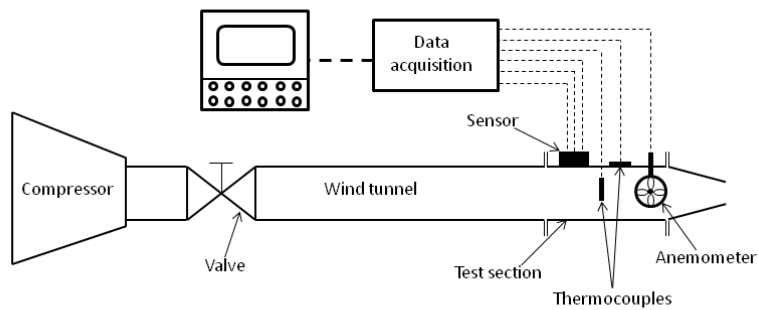
Figure 4: Schematic diagram of the experimental facility (see Ref. [18]).
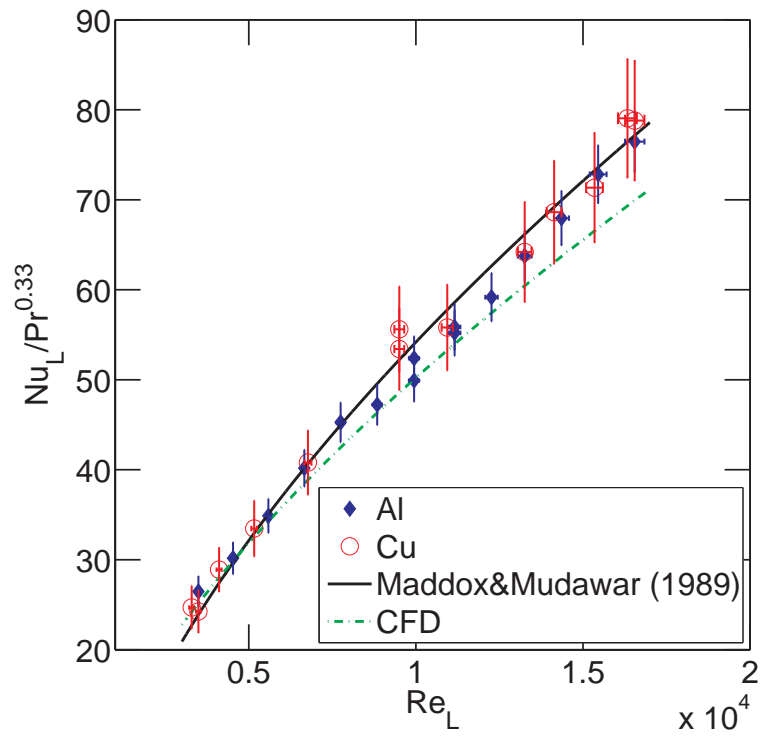
Figure 5: Comparison between experimental data, Maddox&Mudawar experimental correlation[4] and CFD model for aluminum alloy and copper smooth surface.
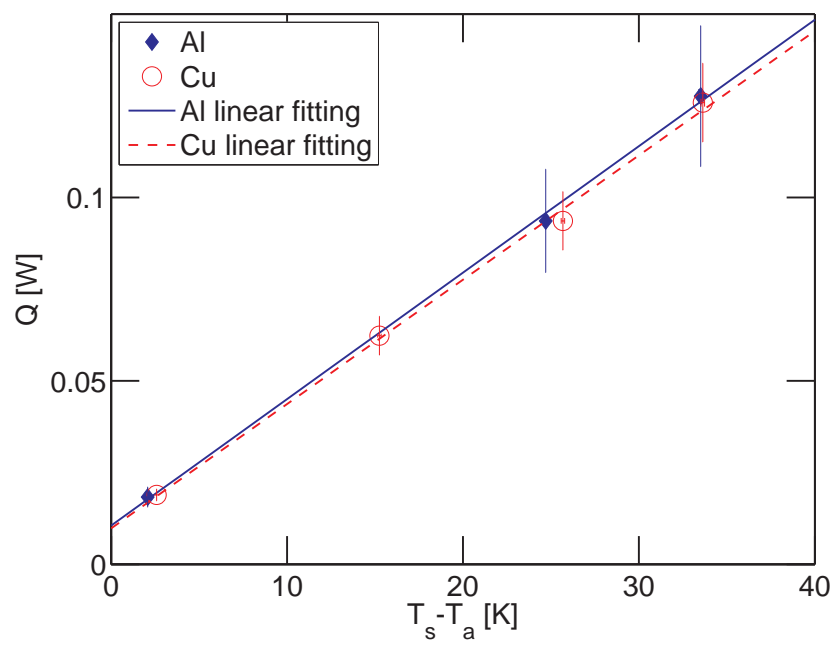
Figure 6: Linear correlation between power given to the sample and temperature difference between the sample and the air for a constant velocity of the air [20].

Figure 7: Examples of micro-structured surfaces: (a) Classical pin-fins, (b) Venturi-like micro-structured pin fins; (c) Rough surface; (d) Rough finned surface. Examples (a) and (b) are discussed in the present work, while examples (c) and (d) are discussed in Ref. [18].
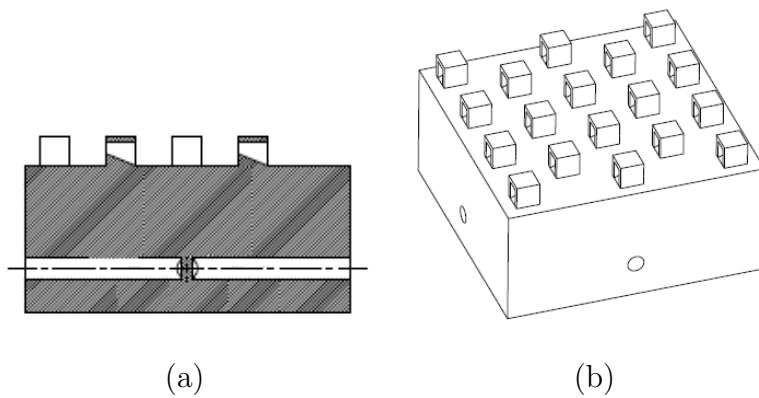
Figure 8: An example with 18 Venturi-like pin fins: (a) Cross section view and (b) isometric view.
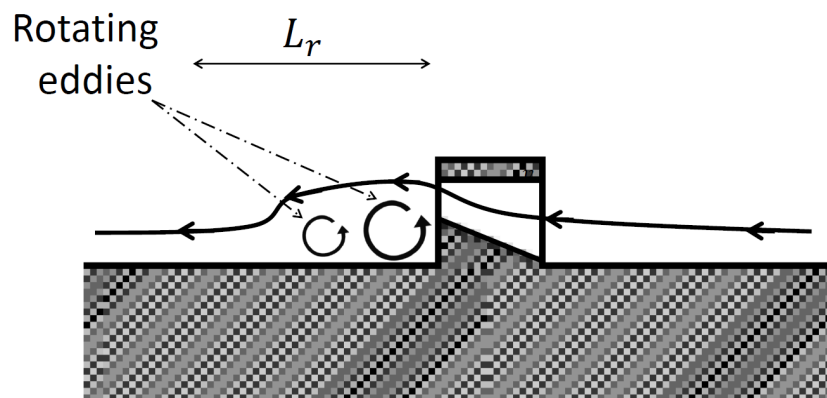
Figure 9: Schematics of the flow field through the Venturi nozzle and near the sample walls downstream. Reattachment length L_r and rotating eddies are sketched.
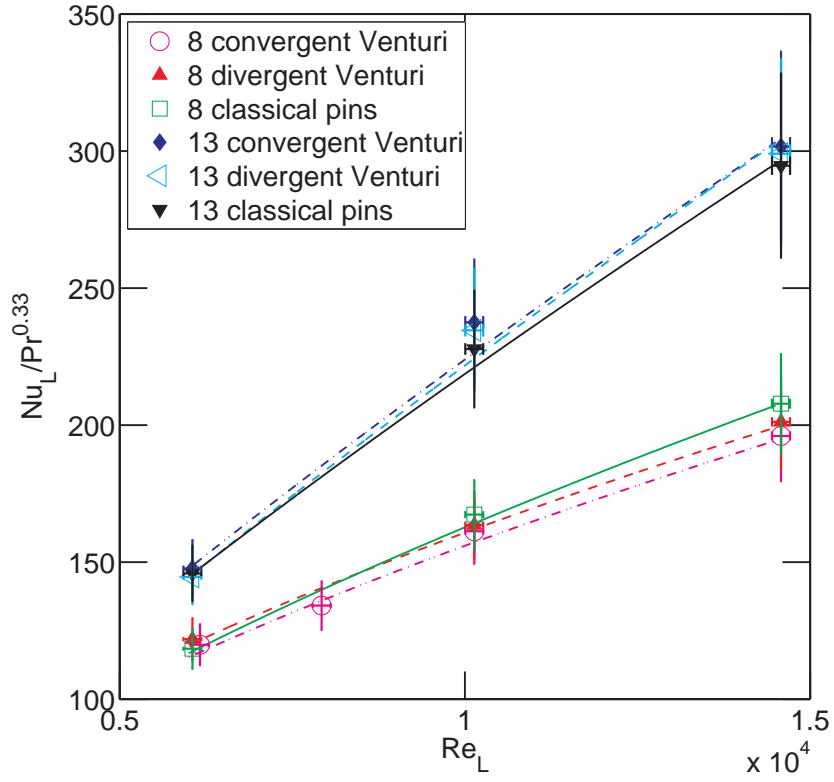
Figure 10: Experimental results of classical versus Venturi-like pin fins (in Eq. (9) $A = 1.123 \times 10^{-4} \ m^2$ for all samples). Power law based fitting curves are shown for convergent Venturi, divergent Venturi and classical pins as dot-dashed, dashed and solid lines, respectively

7. Conclusions and perspectives

In the present paper, a novel sensor for measuring convective heat transfer on small micro-structured surfaces is presented. The key idea is to exploit the notion of thermal guard in order to significantly reduce the effects of spreading heat conduction losses. The maximum and mean estimated relative uncertainties for the convective heat transfer coefficient are found to be $\pm 9.9\%$ and $\pm 6.7\%$, respectively. The experimental results are found to be in good agreement with both experimental data from the literature and a purposely developed computational fluid dynamic model. Maximum and average deviations of the measured Nusselt number from the estimated value by the numerical model are 13.7% and 6.3%, respectively. The comparison of our measurement with literature [4] is even more satisfactory: Maximum and average deviations of Nu_L are found to be 10.7% and 3.4%, respectively.

The evidence that uncertainties due to (spreading) conduction losses can be effectively reduced by the thermal guard implies that no numerical model is required to post-process the measured quantities, and this leads to a direct measurement technique. The sensor can cope with quite small thermal fluxes (i.e. $< 0.2\ W/cm^2$), thus enabling the study of forced air convection on small surfaces (specific thermal fluxes here are order of magnitudes smaller than the one measured in [4]).

Owing to a number of features of the proposed device, we suggest that future studies may focus on the following issues: i) development of a release for industrial applications; ii) high temperature measurements (unlike foil sensors, no delamination issues is experienced); iii) micro-electromechanical systems (MEMS) (easy to miniaturize).

Acknowledgments

A. Computational fluid dynamics (CFD) model

A computational fluid dynamics (CFD) model was used to obtain the mathematical relation between average and axial velocities in the wind channel, i.e. $\mathrm{Re}_D = 0.694\,(\mathrm{Re}_D^x)^{1.0162}$ (see Section 4.2). A rectangular flow channel with the same section as the real one, but much longer entrance length (roughly 60 hydraulic diameters) was considered. The reason being that the constant velocity profile used as inlet condition requires a longer length than real one to develop asymptotically. As a matter of fact, the throttling valve in the real channel is an effective turbulence promoter, which makes the developing length much shorter. The numerical model required roughly 2 millions of computational cells in order to obtain mesh-independent results and a special care was used in meshing the boundary layer. In particular, the maximum y^+ (normalized dimensionless distance of the first cell centroid from the wall) used in the simulations at the maximum Reynolds number was 1.9, i.e. the viscous sublayer ($y^+ < 5$) was correctly meshed [23]. The stan-

dard $k - \epsilon$ turbulence model was adopted for closing the Reynolds-averaged Navier-Stokes (RANS) equations [23]. Because the near-wall mesh was fine enough to resolve the viscous sublayer, the adopted enhanced wall treatment reduces to the traditional two-layer zonal model [23].

A second model has been developed to compute heat transfer coefficient through the sample. The main goal of this second model was to compute the convective heat transfer coefficient h, under different flow conditions. The numerical simulations were used to support the experimental results obtained by the proposed sensor, at least in case of flat surfaces. Fully developed turbulent velocity profile, obtained from the previous model, was imposed at the inlet of the computational domain. The sample and the guard were modeled as an isothermal surface with a temperature higher than that of air, such that the temperature difference $T_s - T_a$ was roughly the same as in the experimental measurements. In this second model, a length of 0.69 m, was considered because the fully developed inlet profiles were already available. The mesh of the cross section was the same as the previous model. On the other hand, a fine homogeneous mesh with 1 mm of grid spacing was chosen along the fluid flow, but close to the upstream edge of the sensor guard, where a finer mesh of 0.1 mm spacing was necessary. These choices granted mesh-independent results. Overall, the above numerical model required roughly 6 millions of computational cells.

For both previous models, some simulations were performed for validation purposes in the following range $3 \times 10^4 \leq \mathrm{Re}_D \leq 17 \times 10^4$ (which is consistent with the experiments reported in this work). Assuming the smooth channels, the numerical results were compared in terms of the Darcy friction factor and

the Nusselt number against the Blasius correlation and Gnielinski correlation, respectively [5]. The maximum deviations between the numerical results and the phenomenological correlations were 6.7 % and 2.1 % respectively.

[1] F.P. Incropera, J.S. Kerby, D.F. Moffatt, and S. Ramadhyani. Convection heat transfer from discrete heat sources in a rectangular channel. *International Journal of Heat and Mass Transfer*, 29:1051–1058, 1986.

[2] C.P. Tso, G.P. Xu, and K.W. Tou. An experimental study on forced convection heat transfer from flush-mounted discrete heat sources. *Journal of Heat Transfer*, 121:326–332, 1999.

[3] H. Bhowmik and K.W. Tou. Experimental study of transient natural convection heat transfer from simulated electronic chips. *Experimental Thermal and Fluid Science*, 29:485–492, 2004.

[4] D.E. Maddox and I. Mudawar. Single- and two-phase convective heat transfer from smooth and enhanced microelectronic heat sources in a rectangular channel. *Journal of Heat Transfer*, 111:1045–1052, 1989.

[5] A. Bejan and A.D. Kraus. *Heat Transfer Handbook*. John Wiley, Hoboken, 2003.

[6] T. Astarita, G. Cardone, G.M. Carlomagno, and C. Meola. A survey on infrared thermography for convective heat transfer measurements. *Optics & Laser Technology*, 32:593–610, 2000.

[7] M. Mori, L. Novak, and M. Sekavcnik. Measurements on rotating blades using ir thermography. *Experimental Thermal and Fluid Science*, 32:387–396, 2007.

[8] H. Ay, J.-Y. Jang, and J.-N. Yeh. Local heat transfer measurements of plate finned-tube heat exchangers by infrared thermography. *International Journal of Heat and Mass Transfer*, 45:4069–4078, 2002.

[9] S. Montelpare and R. Ricci. An experimental method for evaluating the heat transfer coefficient of liquid-cooled short pin fins using infrared thermography. *Experimental Thermal and Fluid Science*, 28:815–824, 2004.

[10] T.S. O'Donovan, T. Persoons, and D.B. Murray. High-resolution hot-film measurement of surface heat flux to an impinging jet. *Meas. Sci. Technol.*, 22:105402, 2011.

[11] H. Mocikat and H. Herwig. Heat Transfer Measurements with Surface Mounted Foil-Sensors in an Active Mode: A Comprehensive Review and a New Design. *Sensors*, 9:3011–3032, 2009.

[12] M. Schwerter, T. Beutel, M. Leester-Schädel, S. Büttgenbach, and A. Dietzel. Flexible hot-film anemometer arrays on curved structures for active flow control on airplane wings. *Microsystem Technologies*, 2014.

[13] EKO Instruments. EKO heat flow sensors. http://eko-eu.com/.

[14] A. Kalani and S.G. Kandlikar. Pool boiling of FC-87 over microchannel surfaces at atmospheric pressure. *Proceedings of the ASME 2012 10th International Mechanical Engineering Congress & Exposition*, 2012.

[15] H. Czichos, T. Saito, and L. Smith. *Handbook of Materials Measurement Methods*. Springer, 2006.

[16] D.G. Holmberg, C.A. Womeldorf, and W.L. Grosshandler. Design and uncertainty analysis of a second-generation convective heat flux calibration facility. *Proceedings of American Society of Mechanical Engineers (ASME) Heat Transfer Division*, 2001.

[17] P.A. Deshmukh and R.M. Warkhedkar. Thermal performance of elliptical pin fin heat sink under combined natural and forced convection. *Experimental Thermal and Fluid Science*, 50:61–68, 2013.

[18] L. Ventola, F. Robotti, M. Dialameh, F. Calignano, D. Manfredi, E. Chiavazzo, and P. Asinari. Rough surfaces with enhanced heat transfer for electronics cooling by direct metal laser sintering. Under consideration of *International Journal of Heat and Mass Transfer*, 2014.

[19] S.J. Kline and F.A. McClintock. Describing uncertainties single-sample experiments. *Mech. Eng.*, 1953.

[20] F. Robotti. *Theoretical analysis and experimental characterization of convective heat transfer enhancement by micro-structured surfaces.* PhD thesis, Politecnico di Torino, 2013.

[21] A. Simchi. Direct laser sintering of metal powders: mechanism, kinetics, and microstructural features. *Materials Science and Engineering: A*, 428:148–158, 2006.

[22] D. Manfredi, F. Calignano, M. Krishnan, R. Canali, E.P. Ambrosio, and E. Atzeni. From Powders to Dense Metal Parts: Characterization of a Commercial AlSiMg Alloy Processed through Direct Metal Laser Sintering. *Materials*, 6:856–869, 2013.

[23] ANSYS FLUENT. 12.0/12.1 documentation, ansys, inc.